JOURNAL OF MATERIALS SCIENCE 31 (1996) 5907–5914

Structural studies of TiN/ZrN multilayer coating deposited by physical vapour deposition

I. WADSWORTH, D. B. LEWIS, G. WILLIAMS
Materials Research Institute, Sheffield Hallam University, Sheffield S1 1WB, UK

Multilayer coatings have been produced using unbalanced magnetron physical vapour deposition in which discrete layers of TiN and ZrN were co-deposited. It has been shown that the multilayers exhibited two-fold periodicity having values of 13 and 2.8 nm. This periodicity, measured both by cross-sectional transmission electron microscopy and low-angle X-ray diffraction, has been precisely related to the process parameters used. Analysis has shown that a third, previously unreported, phase existed within the coating having a lattice parameter comparable to that of TiN and a well-defined orientation relationship with the primary phases. The existence of this phase has been explained in terms of variations in the stoichometry of the coating due to non-uniform metal to nitrogen deposition rates within the chamber. Textural studies revealed that preferred orientation existed in the coating; the degree of which was greater in the ZrN layers than the TiN layers.

1. Introduction

The development of the physical vapour deposition (PVD) process has received much interest, especially as an alternative technology to chemical vapour deposition (CVD) because relatively low deposition temperatures are possible and it is free of noxious by-products. The former is especially pertinent in the area of hard nitride and carbide deposits where the process temperatures must be kept below the tempering temperatures of the high-speed steel substrates being coated.

The early use of diode sputtering was superseded by ion-plating processes in which the deposition rate was increased from 0.2–0.5 $\mathrm{nm\,s^{-1}}$ to up to 5 $\mathrm{nm\,s^{-1}}$ [1], but in order to achieve deposition rates comparable to evaporative processes, balanced magnetron systems were developed [2–4]. These early single cathode systems were not suitable for deposition on to three-dimensional complex substrates owing to the very strong dependence of deposition rate on distance from target [5] and shadowing effects. In addition, the variation in coating composition during reactive sputtering was significant [5]. The incorporation of a double cathode system [5] with subsequent refining [6] served to ameliorate these problems, but only small substrates could be coated. Further developments in the technology were the use of multiple targets and the incorporation of unbalanced magnetrons (UBM) to extend the throwing power of the plasma [7]. A number of workers then exploited this phenomenon in various UBM configurations [8–12] in attempts to deposit uniform coatings on substrates having complex geometry. Subsequently, Teer [13], with a further modification to the design and utilizing single-axis rotation, claimed that routine uniform alloy coating thickness and composition could be achieved on small tools.

Hard wear resistant PVD coatings have now reached the third generation. These superlattice or multilayered coatings have been produced by the alternate deposition of numerous fine layers of two or more compounds [14–18] though metallic interlayers have also been deposited [19]. The mechanisms of hardening in the latter systems are believed either to be due to differences in dislocation line energies or coherency strain fields developed between adjacent layers [16]. The superlattice period, Λ, is known to have an effect on the overall hardness of such coatings. Some recent work has indicated that the improvement in hardness by this mechanism may be synergistic [19].

This paper reports the microstructural characterization of TiZrN films using scanning transmission electron microscopy (STEM) and X-ray diffraction (XRD). Deposition of the films was by unbalanced magnetron (UBM) PVD [11] utilizing two-fold rotation of the substrates. The effect of the second-fold rotation on the periodicity and uniformity of composition and structure of the superlattice layers is illustrated.

2. Experimental procedure

2.1. Fabrication

The coatings were deposited using an HTC 1000-4 ABS™ machine (Fig. 1) manufactured by Hauzer Techno Coating Europe BV [20]; an industrial scale physical vapour deposition machine having dimensions of 1 m corner to corner and a working height of 0.5 m. The desired vacuum was achieved by two Balzers TPH 2200 turbomolecular pumps operating in parallel and backed by a roots blower/rotary pump combination. Radiant heaters mounted on the

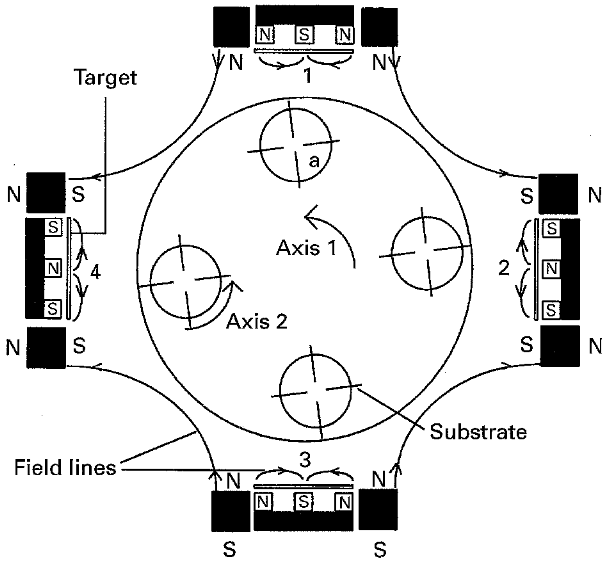

Figure 1 Schematic plan view of the coating unit showing the arrangement and rotation axes of the substrates. The position of the targets and the field generated by the permanent and electro magnet assembly is also illustrated.

chamber walls assisted with chamber out gassing and enabled the substrate temperature to be raised independently of other process variables.

The HTC 1000-4 was equipped with four planar targets (surface area of each target = $190 \times 600\ \text{mm}^2$) mounted at right angles to one another (Fig. 1). For this work three titanium targets (99.98 wt %) and one zirconium target (99.6 wt %) were used. Dual purpose power supplies and magnet arrangements enabled a metal vapour flux to be generated from each target by either sputtering or arc evaporation methods. Running the cathodes in arc mode can be used to pre-treat the substrate prior to an unbalanced magnetron (UBM) sputter-deposited coating. This is the basis of the arc-bond sputter (ABS$^{\text{TM}}$) technique and has been shown to lead to improvements in coating adhesion over conventional UBM-deposited coatings [21]. The four magnetrons utilize Sm/Co permanent magnets and are arranged so that there is magnetic field line linkage between adjacent cathodes to form a closed-field arrangement. Ancillary electromagnets enable the outer poles of each magnetron to be strengthened, thus increasing the degree of unbalancing. This is used to increase the substrate bias current independently of the other process parameters (target power, pressure, bias voltage) and gives added control over the structure and morphology of the deposited coatings.

The substrates used in these trials were 250 mm × 40 mm × 1 mm strips made from a modified 420 grade martensitic stainless steel. Prior to loading into the chamber they were cleaned using a sequence of ultrasonically enhanced alkali decreasing and washing stages followed by de-ionized water rinsing and hot-air drying. Four strips were mounted radially at 90° intervals as shown in Fig. 1 on each of 4 out of the 12 available carousels. After loading, the chamber was pumped down to 1×10^{-5} mbar and heated to 400 °C in order to remove water vapour. A metal ion etch pretreatment of the substrates was performed with a substrate bias voltage $U_b = -1200$ V using the single zirconium target running with an arc current $I_{\text{target}} = 80$ A. A shutter was placed in front of the target in order to minimize droplet contamination of the substrate surface [22]. For the coating phase the three titanium targets and single zirconium target were all run in UBM mode with equal power $P_{\text{target}} = 10$ kW. The substrate bias voltage was held at -75 V. The argon flow during the coating phase was held constant at 220 standard $\text{cm}^3\,\text{min}^{-1}$ and the nitrogen flow was adjusted via a feedback controller to maintain a chamber pressure of 2.74×10^{-3} mbar. These parameters resulted in a process temperature of 400 °C.

The blades underwent two-fold rotation (Fig. 1) during the coating process thus ensuring a uniform thickness over the whole blade. The gearing of the table was such that the carousels rotated on their own axes 3.6 times for every complete rotation of the table. A non-integral ratio is essential in order to maximize the homogeneity of the coating flux across the whole substrate. For these trials, a primary rotation rate of 6.52 cycles min^{-1} was used. Thus during coating, the table rotated approximately 196 times.

2.2. Electron microscopy

Coating thickness was determined by cross-section SEM of fracture surfaces. Detailed examination of the coatings was conducted by scanning transmission electron microscopy (STEM) and energy dispersive X-ray (EDX) analysis in directions both perpendicular to (transverse) and parallel to (plan) the coating growth direction. In the former case, samples were prepared by bonding two sections of coated steel together face to face and coring out 2.8 mm diameter cylinders. These were then inserted and bonded into stainless steel tubes (o.d. = 3 mm) from which 200 μm slices were cut using a diamond-impregnated wire saw. One such disc was ground and polished on one face to a thickness of 50 μm and to a finish of 0.25 μm. The reverse face was further thinned by dimpling, generating a central thickness of 10 μm and to a polish of 0.25 μm. Final thinning to electron translucency was accomplished by argon-ion beam thinning at an incident beam angle of 4°, an accelerating voltage of 5 kV and a current of 7 μA. In order to preserve the coating and interface, the ion beam was only operated at ± 15° to coating growth axis. In the case of the plan sections, 3 mm discs were cut, ground to 50 μm dimpled ground on the steel face as previously described and back ion-beam thinned until a perforation was produced. This provided relatively large translucent areas of substrate free material for study.

The structure and composition of the coating was studied by conventional bright-field (BF) and dark-field (DF) imaging techniques, conical dark-field (CDF) imaging, convergent beam electron diffraction (CBED), and EDX analysis. The spatial resolution for X-ray emission under the conditions used was determined to be of the order of 5 nm.

2.3. Analysis

The composition of the coatings was analysed using both glow discharge optical emission spectroscopy (GDOES) and energy dispersive X-ray (EDX) analysis when studied by STEM.

2.4. X-ray diffraction

The specimens were analysed by XRD using CuK_α radiation in both low- and high-angle configurations using Bragg–Brentano geometry. A direct measurement of the superlattice wavelength, Λ, was made in the low-angle region using the standard Bragg equation

$$\Lambda = \left(\frac{n\lambda}{2\sin\theta}\right) \tag{1}$$

where θ is the Bragg angle and λ is the X-ray wavelength.

The constituent phases, crystallographic textures and lattice parameter measurements were determined by XRD using a Philips diffractometer from θ–2θ scans. The crystallographic texture parameter, P, was calculated from the following standard equation

$$P = \frac{I_{(hkl)}/R_{(hkl)}}{\frac{1}{n}\sum_{0}^{n}(I_{(hkl)}/R_{(hkl)})} \tag{2}$$

where $I_{(hkl)}$ and $R_{(hkl)}$ are the intensities from the (hkl) reflections in the specimen and a random powder, respectively, and n is the number of reflections considered. The coating was found to be comprised of two phases, namely TiN and ZrN, and the P values for each phase were determined. $I_{(hkl)}$ values were determined from the integrated intensity of each (hkl) reflection whilst $R_{(hkl)}$ values were obtained from the JCPDS data of TiN and ZrN [23]. Thus, a P value of 1 signifies a random orientation, whilst for P values greater than 1, the plane is considered to have a preferred orientation. The apparent lattice parameter was calculated from each prominent individual (hkl) reflection for both TiN and ZrN phases and the average value determined.

3. Results

3.1. Cross-sectional studies

SEM observations indicated that the coating was approximately 1 μm thick.

Fig. 2 shows a BF image from a region of a transverse section of coating. Contrasting bands measuring approximately 13 nm and running parallel to the substrate, are clearly visible. Consistency in the band thickness was evident throughout the section, apart from the central region in which they appear to be perturbed, thus modifying the periodicity of composition modulations. This may have been as a result of fluctuations in the drive mechanism. Fig. 3 shows a magnified BF image of a banded region. The figure shows that the bands actually consist of fringes of periodically varying thickness and intensity. The average thickness of the fringes was calculated to be approximately 1.4 nm. It is evident that the dark bands are dominated by thicker, darker fringes and the lighter bands by thinner lighter fringes. Each band pair was found to contain nine fringes.

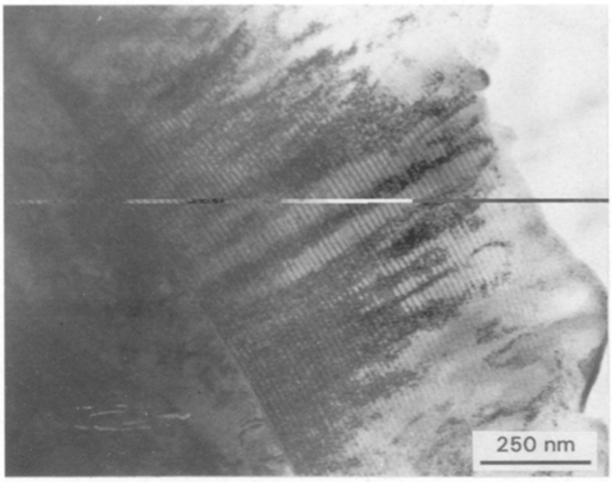

Figure 2 Bright-field TEM image showing a typical region of the coating in cross-section.

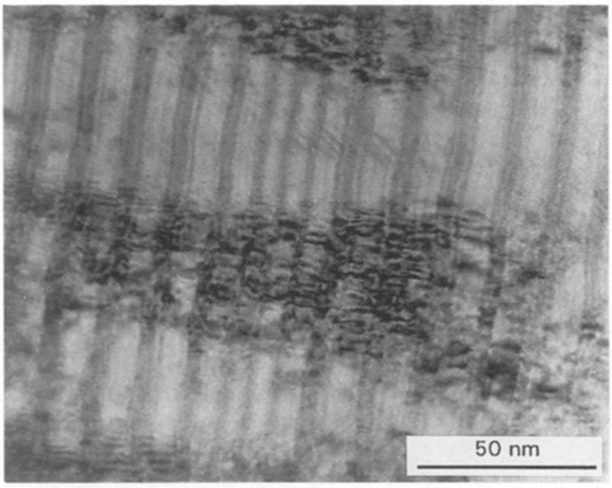

Figure 3 A magnified bright-field image of the coating in cross-section illustrating its periodic nature.

Fig. 4 shows a BF image illustrating the nature of the bands in the proximity of the surface of the coating. Two observations can be made. Firstly, the bands are no longer planar, but are seen to oscillate, tending to follow the coating surface. Secondly, discontinuities in the oscillations are apparent across grain boundaries. This effect is more clearly illustrated in Fig. 5 where two adjacent grains are presented at a higher magnification. The more prominent grain has a pyramidal growth front, and a ⟨1 1 1⟩ growth direction as confirmed by the selected-area diffraction pattern (SADP). The bands may also be seen to mirror the growth surface. Further reference will be made to this SADP in subsequent sections.

As the coating grows, grains having specific orientations (in this case ⟨1 1 1⟩) develop at different rates than adjacent grains of differing orientation. This phenomenon has been observed elsewhere [24]. Consequently, the growth surface becomes increasingly non-planar with deposition time with the multilayers

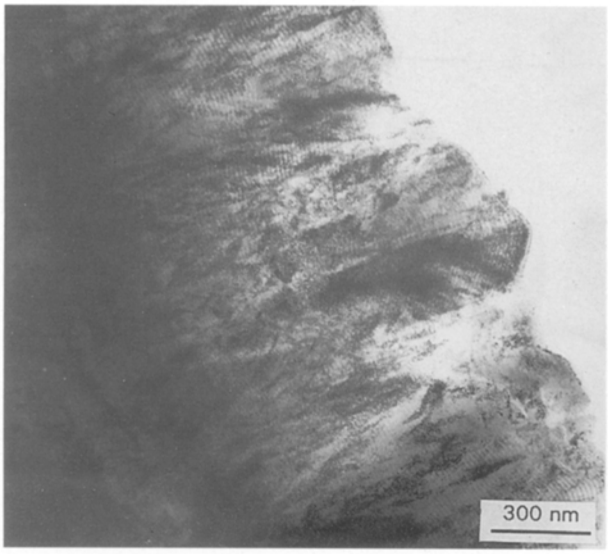

Figure 4 Bright-field image of a transverse section showing the entire coating deposit. The columnar nature of the structure is evident.

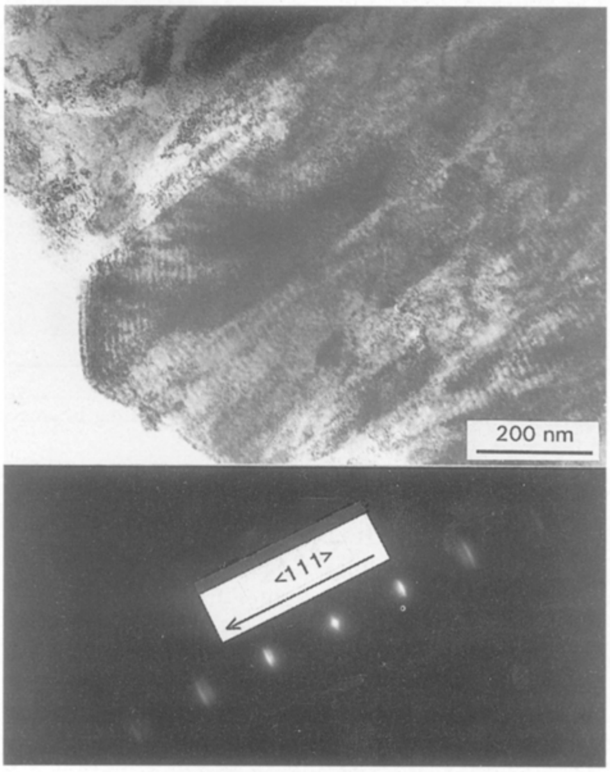

Figure 5 Bright-field image with associated SADP illustrating the morphology and crystallography of the surface of the coating.

mirroring it. Fig. 6 illustrates a BF/DF pair of the interfacial region of a transverse sample. The interface appeared to be diffuse over a region of 10–15 nm. Previous work by Hultman *et al.* [24] has shown that the interface width depends upon the incident ion to metal ratio.

In addition to the above, it may also be noted that the substrate has undergone structural change in the vicinity of the interface. It is likely that this is due to tempering or recrystallization of the martensite structure. Such a phenomenon has been reported elsewhere [25].

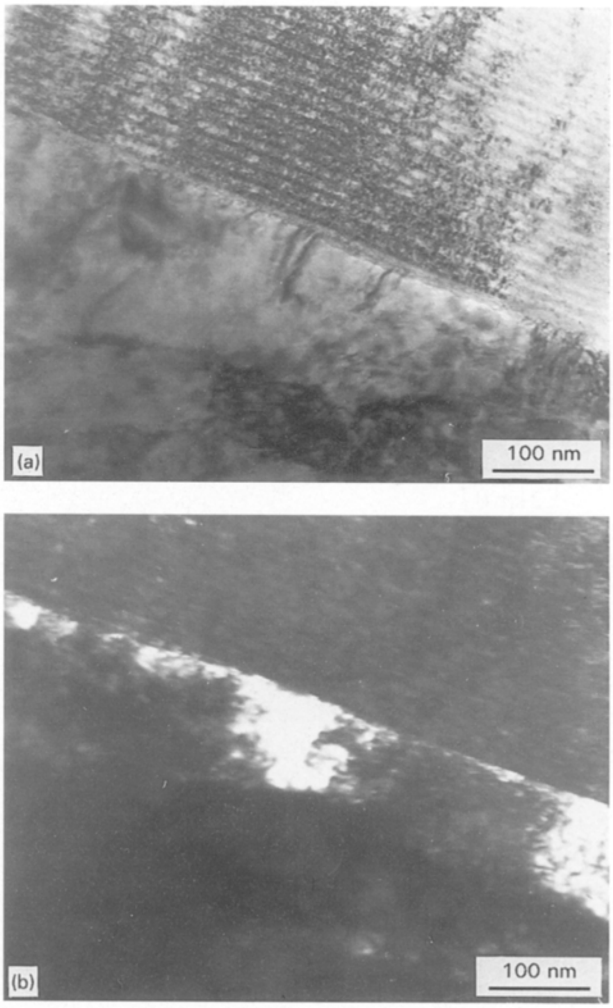

Figure 6 (a, b) Bright-field/dark-field pair illustrating the interfacial region of the substrate–coating couple.

Close inspection of the SADP illustrated in Fig. 5 revealed signs of diffraction in close proximity to the transmitted beam extending in the $\langle 1\,1\,1 \rangle$ direction. Fig. 7 illustrates such a region recorded using an exaggerated camera length. Owing to the extremely low intensity of this diffraction pattern, the image has been computer enhanced. The reciprocal lattice points (RLPs), or streaks in this instance, are oriented in the $\langle 1\,1\,1 \rangle$ direction. The dimensions in real space for these reflections were determined to be 13, 6.5 and 2.9 nm.

Fig. 8 shows a BF/SADP pair illustrating a region in which no contrast due to the columnar grain structure of the coating is evident. However, the banding is clearly visible along with isolated regions of dark contrast. It may be noted that the DP consists of doublets which have been indexed as $\{1\,1\,1\}$ TiN and ZrN reflections with very weak associated "satellite" streaks. A magnified DF image taken using the inner satellite reflection is illustrated in Fig. 9. The poor quality of the image is as a result of the need to use a heavily over focused second condenser lens in order to isolate the desired RLP and the consequential need for an excessive exposure time (100 s) to capture the image. Over this time period, significant specimen drift took place. Nevertheless, the discrete phases are clearly visible.

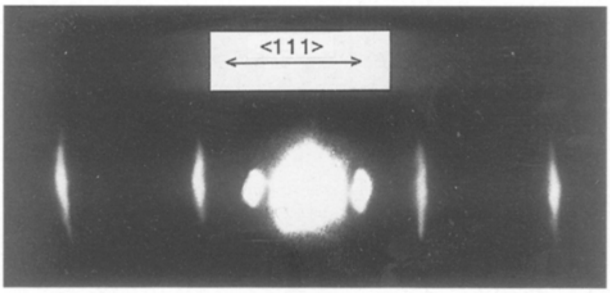

Figure 7 Diffraction pattern taken at an exaggerated camera length to reveal the reflections generated in near-reciprocal lattice space.

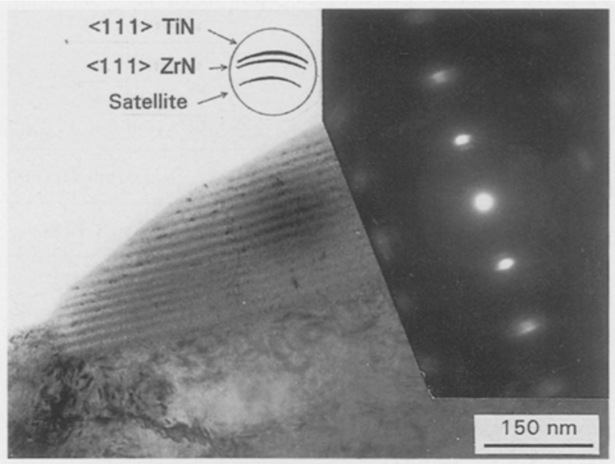

Figure 8 Bright-field transverse image of the basal region of the coating. The associated EDP shows the epitaxial relationship between TiN and ZrN. Weak satellite reflections are also evident. The first-order reflection is illustrated schematically in the insert $\boldsymbol{b} = \langle 1\,1\,2 \rangle$.

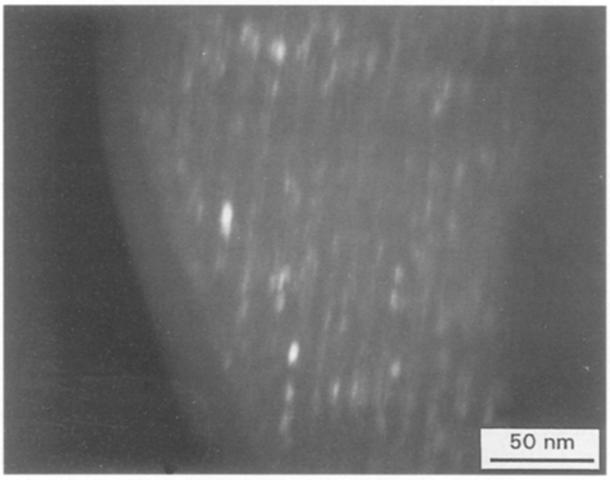

Figure 9 Dark-field image derived from a weak satellite reflection adjacent to $\{1\,1\,1\}$ TiN/ZrN reflections.

3.2. Composition analysis

Quantitative elemental analysis of the coating composition by GDOES gave an average film composition of $Ti_{0.7}Zr_{0.3}N$. For 500 eV argon ion bombardment the sputter yield from titanium is 0.51 whilst from zirconium it is 0.65 [26]. Hence, with three titanium targets and a single zirconium target running at equal power levels the average ratio Ti/Zr would be 2.35:1. This is comparable to the measured ratio Ti/Zr = 2.33. As a consequence of the surface roughness of the substrate, the oscillations of the multilayers and their limited thickness, it was not possible to determine the composition of the fringes, nor the bands which they constituted.

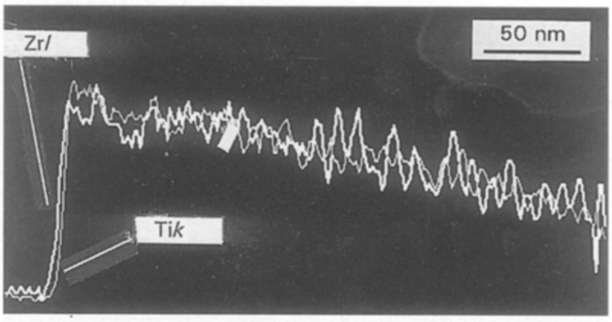

Figure 10 EDX line scan of a cross-section derived from the substrate/coating interface region (left) and extending towards the coating edge.

Fig. 10 illustrates a normalized titanium and zirconium elemental profile across a number of the bands suggesting that, within the limits of resolution, changes in composition were progressive and that the composition maxima were 180° out of phase. The diffuse nature of the fringe boundaries further supports the above.

3.3. Planar studies

A plan section of the coating (i.e. beam direction parallel to the growth direction) is illustrated in Fig. 11. This CDF image was taken about the $\{2\,0\,0\}$ diffraction ring shown in Fig. 12. This image was also computer enhanced in order to ensure reproduction of the weak reflections. The contour line-like pattern may be attributed to buckling of the foil as a result of residual stress relief occurring once the constraint of the matrix was removed during sample preparation. Observations of these plan sections indicated that the maximum grain diameter was of the order of 100 nm.

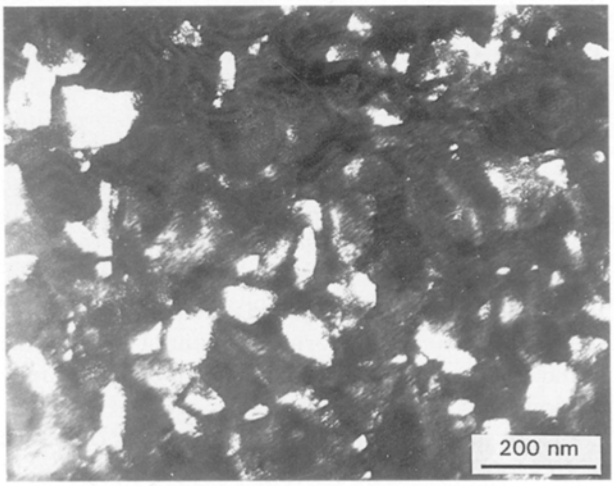

Figure 11 Concal dark-field image of plan section derived from the $\{2\,0\,0\}$ reflections.

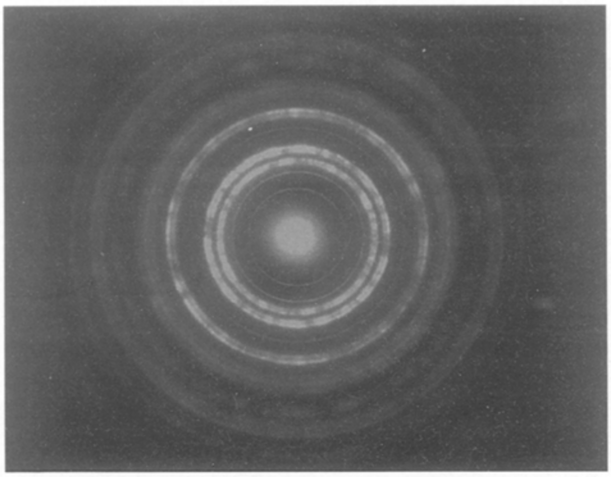

Figure 12 Diffraction pattern derived from a large selected area of a plan section of the coating.

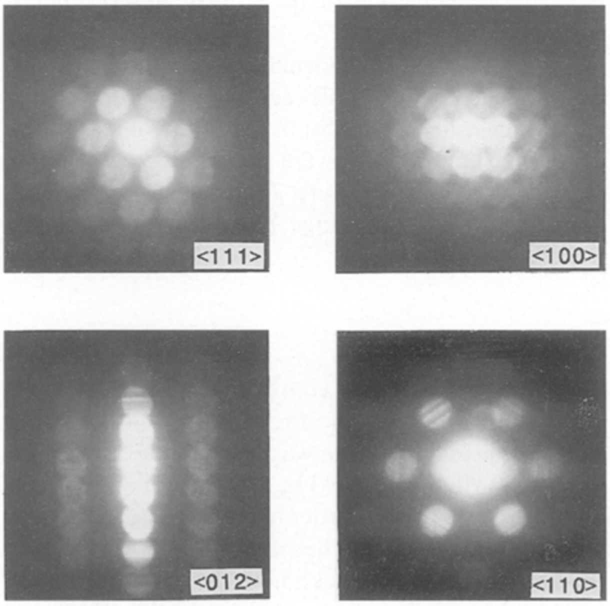

Figure 13 Convergent beam electron diffraction patterns derived from the outer surface of the coating in plan section illustrating typical variations in grain orientation.

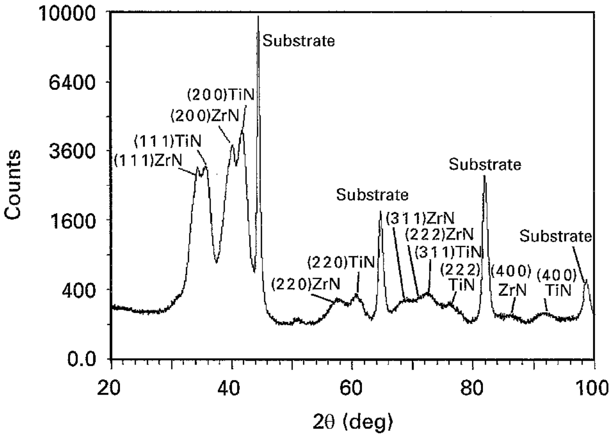

Figure 14 X-ray diffraction trace derived under Bragg–Brentano conditions.

TABLE I X-ray diffraction data for the TiZrN coating

	P				Lattice parameter (nm)	
	(1 1 1)	(2 0 0)	(2 2 0)	(3 1 1)	Sample	JCPDS
TiN	1.23	1.51	0.27	0.99	0.4317	0.4242
ZrN	1.05	2.12	0.31	0.50	0.4520	0.4578

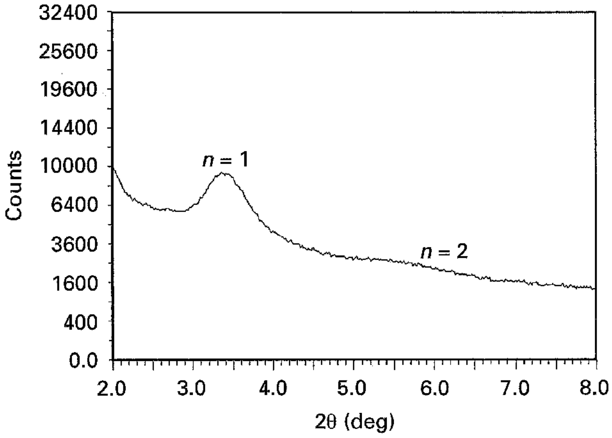

Figure 15 Low-angle X-ray diffraction trace of the same coating showing both first and second order superlattice reflections.

Several observations may be made from the DP shown in Fig. 12. Firstly, strong concentric rings occur as doublets. These are related to the fcc reflections of TiN and ZrN. Secondly, very weak rings are also present whose positions cannot be related to any documented phase containing titanium, zirconium and nitrogen.

Fig. 13 shows a series of CBEDPs in which the defined beam direction represents the most commonly observed growth directions of grains within the coating. As a result of the method of sample preparation, the translucent regions occurred at the outer surface of the coating. Thus this information cannot relate to the initial stages of growth where other orientations may predominate [24].

Fig. 14 shows an XRD trace derived over the range of 20°–100° 2θ in which the separation of the TiN and ZrN phases is clearly evident. The additional peaks are due to the steel substrate. It is also apparent that the peaks from the coating are displaced from their nominal ASTM positions such that the inter-planar spacing of the TiN are greater than predicted and those of the ZrN are less than predicted. Lattice parameter measurements on TiN and ZrN layers together with JCPDS data are shown in Table I. Textural measurements on TiN and ZrN phases are also included in Table I. The ZrN component of the film exhibited a $\{1\,0\,0\}$ texture with a *P* value of 2.12. In the TiN component, however, the $\{1\,0\,0\}$ texture was weaker (*P* value 1.51) and a minor $\{1\,1\,1\}$ texture was also present.

Line-width measurements on the $\{1\,1\,1\}$ reflections showed that the ZrN layers exhibited more broadening than the TiN layers, i.e. full-width at half-maximum (FWHM) of 2.05° of 2θ and 1.38° of 2θ for ZrN and TiN, respectively, thus indicating higher lattice strain and/or grain-size effects.

Fig. 15 shows a low-angle XRD trace in which first- and second-order reflections are shown indicating a superlattice period of 2.6 nm.

4. Discussion

4.1. Development of coating and multilayers

Because the coating was approximately 1 μm thick and the process was 30 min in duration, the average deposition rate may be taken as 0.5–0.6 nm s^{-1}. This rate corresponds to approximately 5 nm per primary revolution. As the table rotates the substrates, in turn, pass in front of the three titanium targets and then the single zirconium target. However, due to the secondary rotation of the carousels they will not be at the same angle to the metal flux on each pass. For a blade positioned directly in front of a target, a sequence of five primary rotations, corresponding to 18 (5×3.6) secondary rotations, is necessary to bring it back to precisely the same position. However, due to the loading configuration (Fig. 1), each substrate was subjected to simultaneous bombardment, albeit at different rates, from opposing targets (see, for example, substrate "a" with respect to targets 2 and 4). This phenomenon promoted beating at twice the frequency; namely 2.5 primary rotations.

The existence of the bands and their constituent fringes are inextricably linked to the deposition process itself. It may be expected that the repeat cycle would be some function of the table and carousel frequencies. Physical measurement of the features from transverse transmission electron micrographs showed that the average band period, Λ_b, was approximately 13 nm and that of the fringes, Λ_f, was 2.8 nm; that is, nine fringes existed per band pair, indicating a band to fringe ratio of 4.5:1. These data show that the band period is generated over 2.5 table rotations and 9 carousel rotations giving approximately 13 nm deposition. In such a case, a substrate directly facing and in closest proximity to a given target will be placed in an identical position with respect to the diametrically opposed target. From this information, therefore, it is evident that the development of the fringes is due to integral secondary rotations of the substrate, hence explaining the observed fringe to band ratio of 4.5:1.

Measurement of the superlattice reflections observed in the TEM EDPs (Fig. 8) gives reflections at 13, 6.5 and 2.9 nm. It is evident from these data that they are not superlattice reflections of orders 1, 2 and 3, respectively. It is apparent that the former two are first- and second-order reflections due to the band period, Λ_b, and that the latter is a first-order reflection due to the fringe period, Λ_f. It should be noted that the ratio of the two first-order reflections is also 4.5:1; the same as that of the band:fringe ratio.

The low-angle XRD data (Fig. 15) compliments the above, indicating both the first- and second-order fringe reflections. It is generally accepted that the broadening of the X-ray peaks from such coatings is due to interfacial roughness and intermixing across phase boundaries [27].

4.2. Coating structure

4.2.1. Preferred orientation

Textural analysis (Table I) indicated that the coatings exhibited a $\{100\}$ preferred orientation. Previous work [28, 29] has shown that superlattice/multilayered structures with periods of around 3.0 nm have a $\{100\}$ texture. This may be explained by the initial film growth starting with a predominately $\{100\}$ orientation [24, 30]. Competitive growth results in the development of other orientations. This would clearly indicate that re-nucleation occurs as confirmed by the dark-field image (Fig. 11). The CBEDPs shown in Fig. 13 indicate several orientations existed on the outer surface of the coating.

4.2.2. Phase analysis and orientation relationships

Analysis of the XRD trace (Fig. 14) indicated the existence of discrete TiN and ZrN phases which are displaced from the equilibrium positions. This deviation may be in part due to some mixing of the impinging species from both targets. The lattice parameter of such alloys is composition dependent, obeying Vegards Law [31]. Another possible additional contribution to the deviation from the equilibrium lattice parameter positions is a mutual constraint mechanism [28] resulting from a combination of opposing residual stresses.

The existence of additional weak reflections in the EDP from plan sections shown in Fig. 12 suggest that they were due to forbidden fcc reflections, being in identical positions to the $\{100\}$, $\{110\}$, $\{211\}$, etc., TiN positions and inferring the possible existence of long-range ordering, LRO. The streaking observed in the RLPs has been explained in terms of the slight variation in orientation of the grains during the growth process [24]. In this case, a further contribution is expected from the oscillations in the coating layers.

In the case of TiZrN alloys, no work has been published on the existence of a true superlattice structure, but ordering is known to occur in TiAlN alloys in which Ti_3AlN forms a Perovskite structure [32]. With reference to Fig. 8, however, it is apparent that LRO cannot be responsible for the additional reflections, because, if the two additional reflections are indeed superlattice reflections of the type $\{110\}$ and $\{211\}$, much stronger fundamental $\{220\}$ and $\{422\}$ reflections would occur in the DP. There is no evidence for their existence. These $\{110\}$ and $\{211\}$ reflections are also parallel to those of the primary $\{111\}$ and $\{220\}$ TiN/ZrN planes, respectively, which cannot occur in a single-phase material. It appears, therefore, that the coating consists of coherent primary TiN and ZrN where $\langle 111 \rangle_{TiN} \| \langle 111 \rangle_{ZrN}$ and an additional discrete phase (c) having the orientation relationship $\langle 110 \rangle_c \| \langle 111 \rangle_{TiN}$ and $\langle 211 \rangle_c \| \langle 110 \rangle_{TiN}$. Because the additional rings produced in the DP shown in Fig. 12 all conform to the position of "forbidden" fcc reflections, it may be surmised that phase c has a cubic structure with a similar lattice parameter to TiN in which non-fcc type of diffraction can take place. The implication is that under the conditions of the process used, a non-equilibrium defective structure developed within the coating suggesting that the deposition process was non-uniform.

5. Conclusions

1. The multilayer coating has been found to consist of a double period structure having wavelengths $\Lambda_b = 13$ nm and $\Lambda_f = 2.8$ nm. Both XRD and ED studies have exhibited excellent correlation with the periodicity observed in the coating.

2. The growth of each fringe has been related to one complete secondary rotation and each band to 2.5 primary rotations of the substrate.

3. The coating was found to consist of discrete layers of epitaxial TiN- and ZrN-rich solid solutions. In addition, a discrete phase exhibiting cubic diffraction behaviour was identified. This phase has been found to have a comparable lattice parameter to TiN and an orientation relationship of $\langle 1\,1\,0\rangle_c \| \langle 1\,1\,1\rangle_{TiN}$. The electron diffraction pattern suggests a defective fcc lattice.

4. Under the conditions used, the ratio of the metal to nitrogen deposition was not constant.

5. The bulk composition of the coating compared well with predictions based on known sputter rates of the target elements.

6. Evidence of preferred orientation was found in the coating. A higher degree of texturing was evident in the zirconium-rich layers.

References

1. A. C. RAGHURAM and R. F. BUNSHAH, *J. Vac. Sci. Technol.* **10** (1972) 1389.
2. A. J. ARONSON, D. CHEN and W. H. CLASS, *Thin Solid Films* **72** (1980) 535.
3. W.-D. MÜNZ, D. HOFMANN and K. HARTIG, *ibid* **96** (1982) 79.
4. W. D. SPROUL, *ibid* **107** (1983) 141.
5. W.-D. MÜNZ and G. HEßBERGER, *Vac. Technik* **30** (1981) 78.
6. *idem*, *US Pat.* 4426 267 (1981).
7. B. WINDOW and N. SAVVIDES, *J. Vac. Sci. Technol.* **A4** (2) (1986) 196.
8. D. TEER, *Surf. Coat. Technol.* **36** (1988) 901.
9. A. G. SPENCER, K. OKO, R. W. LEWIN and R. P. HOWSON, *Vacuum* **38** (1988) 857.
10. J. MUSIL, S. KADELEC, J. VYSKOCIL and V. POULEK, *Surf. Coat. Technol.* **39/40** (1989) 301.
11. W.-D. MÜNZ, D. SCHULZE and F. J. M. HAUZER, *ibid* **50** (1992) 169.
12. W. D. SPROUL, P. J. RUDNIK, M. E. GRAHAM and S. L. RHODE, *ibid.* **43/44** (1990) 270.
13. D. TEER, *ibid.* **39/40** (1989) 565.
14. U. HELMERSSON, S. TODOROVA, S. A. BARNETT, J.-E. SUNDGREN, L. C. MARKERT and J. E. GREENE, *J. Appl. Phys.* **62** (1987) 481.
15. P. B. MIRKARIMI, L. HULTMAN and S. A. BARNETT, *Appl. Phys. Lett.* **57** (25) (1990) 2654.
16. M. SHINN, L. HULTMAN and S. A. BARNETT, *J. Mater. Res.* **7** (1992) 901.
17. X. CHU, M. S. WONG, W. D. SPROUL, S. L. RHODE and S. A. BARNETT, *J. Vac. Sci. Technol.* **A10** (1992) 1604.
18. X. CHU, S. A. BARNETT, M. S. WONG and W. D. SPROUL, *Surf. Coat. Technol.* **57** (1993) 13.
19. X. CHU, M. S. WONG, W. D. SPROUL and S. A. BARNETT, *ibid.* **61** (1993) 251.
20. W.-D. MÜNZ, F. J. M. HAUZER, D. SCHULZE and B. BUIL, *ibid.* **49** (1991) 161.
21. W.-D. MÜNZ, K. VANNISSELROY, R. TIETEMA, T. HURKMANS and G. KEIREN, *ibid* **58** (1993) 205.
22. W.-D. MÜNZ, T. HURKMANS, G. KEIREN and T. TRINH, *J. Vac. Sci. Technol.* **A11** (1993) 2583.
23. JCPDS Index Nos 38-1420 and 35-0753 (International Centre for Diffraction Data, PA, 1993).
24. L. HULTMAN, W. -D. MÜNZ, J. MUSIL, S. KADLEC, I. PETROV and J. E. GREENE, *J. Vac. Sci. Technol* **A9** (1991) 434.
25. G. HÅKANSSON, L. HULTMAN, J.-E. SUNDGREN, J. E. GREENE and W.-D. MÜNZ, *Surf. Coat. Technol.* **48** (1991) 51.
26. J. L. VOSSEN and J. J. CUOMO, in "Thin Film Processes", edited by J. L. Vossen and W. Kern (Academic Press, London, 1978) pp. 12–73.
27. G. HÅKANSSON, L. BIRCH, L. HULTMAN, I. P. IVANOV, J.-E. SUNDGREN and L. R. WALLENBERG, *J. Cryst. Growth* **121** (1992) 399.
28. L. A. DONOHUE, J. CAWLEY, D. B. LEWIS, J. S. BROOKS and W.-D. MÜNZ, *Surf. Coat. Technol* **76/77** (1995) 149.
29. T. HURKMANS, T. TRINH, D. B. LEWIS, J. S. BROOKS and W.-D. MÜNZ, *ibid.* **76/77** (1995) 159.
30. D. S. RICKERBY, A. M. JONES and B. A. BELLAMY, *ibid.* **37** (1989) 111.
31. L. A. DONAHUE, J. CAWLEY and J. S. BROOKS, *ibid.* **72** (1995) 128.
32. JCPDS Index No. 37-1140 (International Centre for Diffraction Data, PA, 1993).

Received 16 February
and accepted 18 March 1996